APS physics

CHORUS

This is the accepted manuscript made available via CHORUS. The article has been published as:

Large magnetoresistance of a compensated metal math xmlns="http://www.w3.org/1998/Math/MathML">mrow>msub>mi>Cu/mi>mn>2/mn>/msub>mi>Sb/mi>/mrow>/math> correlated with its Fermi surface topology

Mizuki Endo, Hideyuki Kawasoko, Seigo Soma, Kunihiko Yamauchi, Miho Kitamura, Koji Horiba, Hiroshi Kumigashira, Noriaki Kimura, Tamio Oguchi, Takafumi Sato, and Tomoteru Fukumura

Phys. Rev. Materials **5**, 105002 — Published 6 October 2021

DOI: 10.1103/PhysRevMaterials.5.105002

Large magnetoresistance of a compensated metal Cu_2Sb correlated with its Fermi surface topology

Mizuki Endo,[1] Hideyuki Kawasoko,[1] Seigo Soma,[2,3,4], Kunihiko Yamauchi,[5,6] Miho Kitamura,[7] Koji Horiba,[7] Hiroshi Kumigashira,[7,8] Noriaki Kimura,[9] Tamio Oguchi,[5] Takafumi Sato,[2,3,4,9*] and Tomoteru Fukumura[1,2,3,4*]

[1]Department of Chemistry, Graduate School of Science, Tohoku University, Sendai 980-8578, Japan

[2]Center for Spintronics Research Network, Tohoku University, Sendai 980-8577, Japan

[3]Advanced Institute for Materials Research and Core Research Cluster, Tohoku University, Sendai 980-8577, Japan

[4]Center for Science and Innovation in Spintronics, Organization for Advanced Studies, Tohoku University, Sendai 980-8577, Japan

[5]Institute of Scientific and Industrial Research (ISIR), Osaka University, Ibaraki, Osaka 567-0047, Japan

[6]Center for the Promotion of Interdisciplinary Education and Research (CPIER), Kyoto University, Kyoto 606-8317, Japan

[7]Institute of Materials Structure Science, High Energy Accelerator Research Organization, Tsukuba, Ibaraki 305-0801, Japan

[8]Institute of Multidisciplinary Research for Advanced Materials, Tohoku University, Sendai 980-8577, Japan

[9]Department of Physics, Graduate School of Science, Tohoku University, Sendai 980-8578, Japan

* tomoteru.fukumura.e4@tohoku.ac.jp

* t-sato@arpes.phys.tohoku.ac.jp

Abstract

We report electrical transport properties and electronic structure of a nonmagnetic metal Cu_2Sb single crystal. Cu_2Sb was found to be a compensated metal with high carrier density ~10^{22} cm^{-3} and high carrier mobility $\geq$ 10^3 cm^2/Vs for both electron and hole carriers. The current-in-plane magnetoresistance at 2 K and 9 T was 730%, while the current-perpendicular-to-plane magnetoresistance at 2 K and 9 T was 2700% without the saturation. Angle-resolved photoemission spectroscopy throughout the three-dimensional (3D) bulk Brillouin zone signified a quasi-two-dimensional (2D) electron pocket axially-centered along the M-A line and a 3D hole pocket at the Γ point, in accordance with the electron-hole compensated nature. The presence of quasi-2D open Fermi surface, in line with the first-principles band-structure calculations, is likely responsible for the observed non-saturating current-in-plane magnetoresistance. The present result lays the foundation for realizing large magnetoresistance via Fermiology engineering in compensated metals.

Introduction

Recently, large magnetoresistance (MR) was discovered in nonmagnetic materials such as $PdCoO_2$, WTe_2, and LaSb [1–3]. The large MR has been considered to originate from non-saturating behavior at high magnetic field, which caused by either open Fermi surface or electron-hole compensation, in addition to high carrier mobility [4–9]. The former was proposed for current-perpendicular-to-plane (CPP) MR of $PdCoO_2$ with open Fermi surface along k_z direction [1,4], while the latter was proposed in various semimetallic compounds such as WTe_2 and LaSb [10–13].

Cu_2Sb is a layered compound composed of alternating stack of Cu square net and CuSb block layer [Fig. 1(a)], and was reported to be a nonmagnetic metal exhibiting current-in-plane (CIP) MR of around 1000% at 4 K and 9 T more than 45 years ago [14–18], attributed to the open Fermi surface along k_x direction [18,19]. Although Cu_2Sb was suggested to be a compensated metal [18,19], the effect of electron-hole compensation in Cu_2Sb has been unclear since the fundamental electrical properties such as the carrier polarity, density, and mobility were not investigated. In addition, a quasi two-

dimensional (2D) Fermi surface confirmed by the de Hass-van Alphen effect and the band calculation indicated the presence of open Fermi surface along k_z direction [17,19,20], suggesting a possible large CPP-MR in Cu_2Sb.

In this study, we synthesized Cu_2Sb single crystal, and evaluated the electrical transport properties and the band structure by angle-resolved photoemission spectroscopy (ARPES). Cu_2Sb was found to be a compensated metal with high electron and hole carrier density $\sim 10^{22}$ cm^{-3}, representing that electron-hole compensation resulted in the observed large CIP-MR. Furthermore, the CPP-MR of 2700% at 2 K and 9 T was considerably larger than the CIP-MR of 730% probably as a result of open Fermi surface along the k_z direction, which was directly confirmed by the bulk-sensitive soft-x-ray (SX) ARPES measurements.

Experimental method

Cu_2Sb single crystals were grown by melt growth method with Cu_2Sb polycrystal as follows. The Cu_2Sb polycrystal was synthesized by sintering mixed powders of Cu (99.99%) and Sb (99.99%) in an evacuated quartz tube at 500 °C for 48 h. The Cu_2Sb single crystal was synthesized using the Cu_2Sb polycrystal powder as follows. The powder was heated in an evacuated quartz tube to 500 °C with a rate of 50 °C/h, then to 700 °C with a rate of 100 °C/h, kept at 700 °C for 48 h, cooled down to 500 °C with a rate of 2 °C/h, and quenched to room temperature. The crystal structure was evaluated by x-ray diffraction (XRD) with Cu Kα radiation (D8 DISCOVER, Bruker AXS). The crystal parameters were determined by Rietveld analysis with RIETAN-FP [21] on the powder XRD. The crystal structures were drawn with the VESTA [22]. The chemical composition was evaluated by scanning electron microscopy equipped with energy dispersive x-ray spectroscopy (SEM-EDX; S-4300, HITACHI). The electrical transport properties were measured by physical property measurement system (PPMS; Quantum Design) and a cryostat equipped with dilution refrigerator (Kelvinox TLM, Oxford). The magnetic properties were measured by magnetic property measurement system (MPMS; Quantum Design). The band structure was evaluated by ARPES. Vacuum ultraviolet (VUV) ARPES

measurements were performed with a DA30 electron analyzer with micro-focused synchrotron light at BL-28 in Photon Factory. We used circularly polarized light of 60–80 eV. SX-ARPES measurements were performed at BL-2 (MUSASHI) in Photon Factory with 250–500 eV photons with horizontal linear polarization. The energy resolutions for VUV- and SX- ARPES measurements were set to be 10–30 and 150 meV, respectively. Samples were cleaved *in situ* along the *ab*-plane in an ultrahigh vacuum of 1×10^{-10} Torr, and kept at T = 13 K or 40 K during the measurements. Electronic band-structure calculations were carried out by means of a first-principles density-functional-theory approach by using the all-electron full-potential linearized-augmented-plane-wave (FLAPW) program package HiLAPW [23]. The self-consistent calculations were performed by using GGA exchange-correlation potential [24] and the FLAPW basis set with the scalar-relativistic scheme and the improved tetrahedron integration method [25] up to 16×16×12 $\boldsymbol{k}$-mesh points in the Brillouin zone. The lattice parameters and atomic positions were fixed at their experimental values. The spin-orbit coupling was included in second variation. The calculated energy dispersion was fitted with symmetrized star functions by a spline method with 64×64×48 $\boldsymbol{k}$-mesh points and used for calculations of the Fermi surfaces. The Fermi surfaces were drawn with the FermiSurfer [26].

Results and discussion

Figure 1(b) shows the XRD pattern of Cu_2Sb single crystal. All peaks were attributed to the Cu_2Sb 00*l* diffractions. A photograph of Cu_2Sb single crystal with cleaved *ab*-plane is shown in the inset of Fig. 1(b). From Rietveld analysis on the powder XRD at room temperature, the crystal structure of Cu_2Sb was confirmed to be tetragonal (*P*4/*nmm*) with the lattice constants of a = 4.001 Å and c = 6.103 Å (Fig. S1 and Table S1 in the Supplemental Material [27]), consistent with the previous study (a = 4.001 Å, c = 6.104 Å) [14]. From the EDX measurement, the chemical composition of Cu:Sb was 2.0:1.0, indicating the stoichiometric composition of Cu_2Sb single crystal.

Figure 2(a) shows the temperature dependence of in-plane resistivity along *a*-axis (ρ_{xx}). The ρ_{xx} showed a metallic conduction with the residual resistivity of 56 nΩcm below 10 K at 0 T,

corresponding to the residual resistance ratio (RRR: ρ_{xx} (300 K)/ρ_{xx} (2K)) of 135, comparable to the previous study (RRR = 180) [18]. Here, no superconducting transition was observed down to 22 mK [the inset of Fig. 2(a)], contrary to a superconducting transition at 85 mK reported previously [15]. At magnetic field of 9 T along the *c*-axis, the ρ_{xx} significantly increased below ~60 K with a local minimum at 24 K. Figure 2(b) shows CIP-MR, $\rho_{xx}(H)$, at various temperatures. The positive CIP-MR monotonically increased with decreasing temperature down to 10 K and was almost the same for 2−10 K. At 2 K and 9 T, the CIP-MR was 730% [$\Delta\rho_{xx}/\rho_{xx}$ in the inset of Fig. 2(b)], similar to the previous study (~1000%) [18]. The negative and temperature independent magnetic susceptibility of Cu_2Sb from 2 to 300 K showed the absence of magnetic transition above 2 K (Fig. S2 in the Supplemental Material [27]) as reported previously [14–16], representing that the observed large MR was not magnetic origin. An antiferromagnetic transition at 373 K in previous study [28] was probably caused by magnetic impurities.

Figure 2(c) shows the magnetic field dependence of Hall resistivity (ρ_{yx}) at various temperatures. The ρ_{yx} was evaluated by extracting the odd component of Hall resistance (Fig. S3 in the Supplemental Material [27]) with respect to magnetic field to remove the contribution of MR. The non-linear magnetic field dependence of ρ_{yx} was apparent below 30 K, indicating the presence of both electron and hole carriers. By using two-carrier model with a pair of electron and hole carriers [29], the carrier density and mobility at each temperature were evaluated. The fitting of $\rho_{yx}(H)$ and $\rho_{xx}(H)$ was performed above 30 K [Table S2(a) and Fig. S4 in the Supplemental Material [27]], while the fitting of only $\rho_{yx}(H)$ was performed below 20 K [Table S2(b) and Fig. S5 in the Supplemental Material [27]] due to these better fitting attributed to the presence of linear magnetoresistance component (Fig. S4 in the Supplemental Material [27]). As shown in Fig. 2(d), the high carrier density of electron and hole with the order of 10^{22} cm^{-3} was confirmed, indicating that the electron and hole carriers were compensated. The hole carrier density showed the slight enhancement below 30 K, while the electron carrier density was almost independent of temperature. The electron and hole mobility increased with decreasing temperature, and reached up to 3400 $cm^2V^{-1}s^{-1}$ and 2200 $cm^2V^{-1}s^{-1}$, respectively, at 2 K

[Fig. 2(e)]. Taking into account these results, the high mobility mainly contributed to the large CIP-MR in addition to a partial compensation of electron and hole carriers.

Figure 3(a) shows the temperature dependence of out-of-plane resistivity along *c*-axis (ρ_{zz}). At 0 T, the ρ_{zz} was about three times larger than the ρ_{xx} with the similar temperature dependence [Fig. 2(a)], reflecting the quasi-2D open Fermi surface of Cu_2Sb as discussed below (Fig. 4). At 9 T along the *a*-axis, the ρ_{zz} was increased up to ~5 μΩcm at 2 K, which was ten times higher than the ρ_{xx} at 2 K. Figure 3(b) shows the CIP-MR ($\Delta\rho_{xx}/\rho_{xx}$) and CPP-MR ($\Delta\rho_{zz}/\rho_{zz}$) at 2 K under the magnetic field along the *c*- and *a*- axis, respectively. In contrast with the gradual increase in the CIP-MR, the CPP-MR rapidly increased to be 2700% at 9 T without saturation, indicating the presence of the open Fermi surface along the k_z direction [17,19,20]. The two-fold and four-fold symmetric angular dependences of CIP- and CPP- MR at 2 K, respectively [Fig. S6 and Fig. 3(c)], reflected the tetragonal crystal symmetry of Cu_2Sb [14]. Several local minima in the angular dependence of CIP- and CPP- MR reflected the complicated Fermi surface topology of Cu_2Sb [17,18]. The CPP-MR was increased up to 4000% by applying magnetic field around the [110] direction [Fig. 3(c)] due to the quasi-2D open Fermi surface of Cu_2Sb axially-centered along the M-A line as discussed below (Figs. 4 and 5).

To examine a relationship between the electrical transport properties and electronic structure, first-principles band-structure calculations were carried out. As shown in Fig. 4(b), the calculated band structure along high-symmetry lines in the bulk Brillouin zone [Fig. 4(a)] display several nearly flat bands around E_B = 3–5 eV, consistent with the previous literature [20]. According to the calculated partial density of states (DOS) in Fig. 4(c), these bands are attributed to the Cu 3*d* orbital and produce several sharp peaks in DOS. The plot in Fig. 4(c) also signifies that the Cu 3*d* orbital largely contributes to the total DOS. As seen from the calculated Fermi-surface plots in Figs. 4(d) and 4(e), there exist six types of bands (labeled here 1–6) that are responsible for the formation of bulk Fermi surface, as suggested in the angular dependence of CIP- and CPP- MR. Specifically, bands 1 and 2 form small 3D hole pockets centered at the R point, and band 3 forms a large hole pocket with occupied electrons at the A–M corner. Band 4 forms a quasi-2D cylindrical Fermi surface axially-centered along the M-A

line together with the small electron pocket at the Z point, and bands 5 and 6 form small 3D electron pockets around the M point. Existence of both electron and hole pockets in Cu_2Sb is consistent with our transport measurement that supports the coexistence of both electron and hole carriers. By integrating DOS in the occupied region, we have estimated the volume of Fermi surface for bands 1–6 to be 1, 5, 30, 35, 0.2, and 0.1 % of 3D Brillouin zone, respectively. Among these bands, band 3 was found to contribute dominantly to the total DOS and calculated Hall coefficient, consistent with the experimental Hall measurement which suggests superior hole carriers at low temperature. Since the Hall coefficient is not only related to the Femi-surface volume but also to the curvature of Fermi surface and DOS at E_F, this hole Fermi surface was found to contribute largely to the Hall coefficient despite the fact that the electron pocket from band 4 is 5% larger than this hole pocket.

The vertical slice of calculated Fermi surface in the ΓMAZ plane in Fig. 5(a) signifies several closed 3D pockets, *i.e.* a large pocket at the Γ point (band 3), a small pocket at the Z point (band 4), and two small pockets at the M point (bands 5 and 6), together with a quasi-2D open Fermi surface axially-centered along the M-A line (band 4). To determine the 3D bulk Fermi surface, ARPES measurements were performed at the normal-emission setup with varying photon energy ($h\nu$) in the SX region (300–375 eV). The ARPES-intensity mapping at E_F in the ΓMAZ plane shown in Fig. 5(b) reveals warped open Fermi surface whose periodicity well matches that of the bulk Brillouin zone. As shown in the corresponding momentum distribution curves (MDCs) at E_F in Fig. 5(c) plotted as a function of in-plane wave vector parallel to the ΓM cut ($k_{//}$), a few peaks originating from different Fermi surfaces are clearly resolved. A peak marked by triangle which originates from band 4 apparently moves its k position upon $h\nu$ variation, demonstrating a finite k_z dispersion and thereby bulk origin of this Fermi surface. A careful look at Fig. 5(c) also reveals weak peaks (vertical dashed lines) whose k position is robust against $h\nu$ variation. These bands may be explained in terms of either the surface state or the k_z broadening effect occurring in the SX region (note that the k_z-broadening effect in the SX and VUV regions can be understood in terms of the electron kinetic energy, the inelastic electron mean-free path, and the angular resolution of electron analyzer, as detailed in

supplemental note S1) [30]. The quasi-2D nature of the pocket axially-centered along the M-A line is also confirmed by the ARPES-intensity mapping at E_F plotted against in-plane wave vector (k_x and k_y) in Fig. 5(d), where one can recognize a large pocket at both $k_z = 0$ and π planes (blue allows) which are smoothly connected to each other upon variation of k_z [Fig. 5(b)]. Overall agreement of the ARPES-intensity distribution and the calculated band structure in Fig. 5(d) strongly suggests that the band calculation is a good starting point to describe the overall electronic structure of Cu_2Sb. It should be emphasized here that, although the existence of open Fermi surface was suggested from the previous studies [17,18], the present study that applies SX-ARPES on Cu_2Sb for the first time unambiguously establishes that such Fermi surface indeed exists; this enables us to conclude that the Fermi surface topology is correlated with the observed non-saturating large CPP-MR (Fig. 3). It is noted that there exist some differences between the ARPES data in Fig. 5(b) and the calculation in Fig. 5(a). For example, a large 3D pocket centered at the Γ point and a small pocket at the Z point predicted in the calculation are not clearly resolved in the experiment, probably because of the intensity suppression due to the photoelectron matrix-element and photoionization cross-section effects as well as the insufficient resolution; this point needs to be further investigated by the future studies with higher accuracy.

To discuss the Fermiology in more detail, VUV-ARPES measurement was performed to determine energy band structure more accurately. Although VUV-ARPES is known to suffer stronger k_z broadening effect associated with the shorter photoelectron mean-free path, it is also useful to determine the band structure with much higher energy and k resolutions. Figures 5(e) and 5(f) show plots of ARPES-determined band dispersions measured along high-symmetry cuts. The same plots but calculated band structure for $k_z = 0$ (solid curves) and π (dashed curves) are superimposed are also shown in Figs. 5(g) and 5(h). One can immediately recognize several sharp features in the ARPES intensity in Figs. 5(e) and 5(f), supportive of the long quasiparticle lifetime, consistent with the high carrier mobility in Fig. 2(e). Although the VUV data at $h\nu = 62$ and 80 eV was expected to reflect information of $k_z = 0$ and π planes, respectively, based on the V_0 value (10.0 eV) estimated from the

periodicity of the band dispersion in the SX data, the ARPES data at both $h\nu$'s suffer strong k_z broadening effect. Specifically, when the ARPES intensity at $h\nu$ = 62 eV is overlaid with the calculated band dispersion for both k_z = 0 (solid curves) and π (dashed curves) in Fig. 5(g), not all of the experimental bands are attributed to the calculated bands at k_z = 0, but some of them show a better matching with the calculated ones at k_z = π (highlighted by green arrows). This is also the case for $h\nu$ = 80 eV shown in Fig. 5(h) (highlighted by blue arrows), and thereby suggests that the k_z broadening is so strong at both $h\nu$ = 62 and 80 eV that the broadening fully covers the k_z = 0 and π plane. Then, the difference in the ARPES intensity profiles between $h\nu$ = 62 and 80 eV would be largely associated with the variation of photoelectron matrix-element effect and photoionization cross-section. The strong k_z broadening is also supported by our MDC analysis in Fig. 5(i) where some peaks in the MDCs at representative E_B slices stay at the same k position between $h\nu$ = 62 and 80 eV. Such $h\nu$ invariance is also visualized by the $h\nu$-dependence of MDCs along the wave vector parallel to the ΓX cut in Fig. 5(j). It is noted that some bands crossing E_F in Figs. 5(e) and 5(f) look fairly sharp despite the significant k_z broadening effect. Although this is likely due to the dominant contribution from the k_z = 0 and π components among different k_z's to the total spectral density of states associated with the presence of band-singularity points (see also supplemental note S1) [31], some of the MDC peaks in Figs. 5(i) and 5(j) may be still too sharp to be fully explained with this picture. Also, spectral weight where the projection of bulk bands exists may be very weak in some (E, **k**) region. These observations suggest a contribution from the 2D surface states with longer-lived quasiparticles at the bulk-band edges.

When the strong k_z broadening effect is taken into account, one can find a direct correspondence between the experiment and calculation in almost all the bands in Figs. 4(g) and 4(h). For example, the calculation nicely reproduces the electron-like band axially-centered along the M-A line (band 4) which crosses E_F at the midway between the Z and A points or Γ and M cuts, being responsible for the aforementioned quasi-2D electron pocket. In addition, the hole-like band crossing E_F around the Γ point forming the 3D hole pocket at Γ (band 3) also shows a good matching between the experiment and calculation. These electron- and hole- like bands show steep dispersion around E_F, contributing to

the high carrier mobility [Fig. 2(e)].

A careful look at Fig. 4(e) also reveals that the calculated small electron pockets (bands 5 and 6) at the M point, bottomed at the binding energy of ~0.2 eV, has no counterpart in the experiment. The absence of this electron pocket was also confirmed by the SX-ARPES measurements down to T = 13 K (Fig. S7 in the Supplemental Material [27]), and it is thereby an intrinsic nature of Cu_2Sb, although the reason is unclear at the moment. It cannot be at least explained in terms of the hole doping into the crystal, because (i) the experimental and calculated band dispersions agree fairly well in other bands, and (ii) electron-hole compensated nature is supported from the electrical transport properties and stoichiometric chemical composition of the single crystal. Electron correlations may play a role to push the electron pockets above E_F, although weakly correlated nature of Cu_2Sb is suggested from the overall agreement of the band structure between experiment and calculation. Actual role of electron correlations needs to be examined by the further studies.

In addition, the origin of a slight enhancement in hole carrier density below T = 40 K revealed in Fig. 2(d) is unclear at the moment, because we found no discernible change in the overall band structure between T = 13 and 40 K in the ARPES data (Fig. S7 in the Supplemental Material [27]). Also, the observed 3D vs 2D nature of hole and electron pockets, respectively, may cause different scattering events between electron and hole carriers, leading to unconventional temperature dependence of carrier density and mobility at low temperatures. Further investigations such as crystal structural analysis at low temperatures are necessary to clarify the relationship between the electrical transport properties and electronic structure at low temperatures.

Conclusion

In summary, Cu_2Sb was found to be a compensated metal, in which the electron and hole carriers were the order of 10^{22} cm^{-3} with high mobility of 3400 $cm^2V^{-1}s^{-1}$ and 2200 $cm^2V^{-1}s^{-1}$, respectively, resulting in the large CIP-MR. As a result of the quasi-2D electronic structure of Cu_2Sb, the ρ_{zz} was larger than the ρ_{xx}. Intriguingly, the CPP-MR showed non-saturating behavior at high magnetic field,

which was four times larger than the CIP-MR. From the ARPES measurement, the quasi-2D electron pocket axially-centered along the M-A line and the 3D hole pocket centered at the Γ point were directly revealed, in good agreement with these electrical transport properties of Cu_2Sb as a compensated metal. These results indicate that the existence of open Fermi surface besides the electron-hole compensation is a key to realize large magnetoresistance in Cu_2Sb.

Acknowledgement

The authors acknowledge Dr. D. Oka for technical support, C.-W. Chuang and T. Kato for their assistance in the ARPES experiments. This study was supported by Yazaki Memorial Foundation for Science and Technology, Iketani Science and Technology Foundation, and JST-CREST (No. JPMJCR18T1).

References

[1] H. Takatsu, J. J. Ishikawa, S. Yonezawa, H. Yoshino, T. Shishidou, T. Oguchi, K. Murata, and Y. Maeno, Extremely large magnetoresistance in the nonmagnetic metal $PdCoO_2$. Phys. Rev. Lett. **111**, 056601 (2013).

[2] M. N. Ali, J. Xiong, S. Flynn, J. Tao, Q. D. Gibson, L. M. Schoop, T. Liang, N. Haldolaarachchige, M. Hirschberger, N. P. Ong, and R. J. Cava, Large, non-saturating magnetoresistance in WTe_2. Nature **514**, 205 (2014).

[3] F. F. Tafti, Q. D. Gibson, S. K. Kushwaha, N. Haldolaarachchige, and R. J. Cava, Resistivity plateau and extreme magnetoresistance in LaSb. Nat. Phys. **12**, 272 (2016).

[4] S. Zhang, Q. Wu, Y. Liu, and O. V. Yazyev, Magnetoresistance from Fermi surface topology. Phys. Rev. B **99**, 035142 (2019).

[5] L.-K. Zeng, R. Lou, D.-S. Wu, Q. N. Xu, P.-J. Guo, L.-Y. Kong, Y.-G. Zhong, J.-Z. Ma, B.-B. Fu, P. Richard, P. Wang, G. T. Liu, L. Lu, Y.-B. Huang, C. Fang, S.-S. Sun, Q. Wang, L. Wang, Y.-G. Shi, H. M. Weng, H.-C. Lei, K. Liu, S.-C. Wang, T. Qian, J.-L. Luo, and H. Ding, Compensated semimetal LaSb with unsaturated magnetoresistance. Phys. Rev. Lett. **117**, 127204 (2016).

[6] Y.-Y. Lv, B.-B. Zhang, X. Li, S.-H. Yao, Y. B. Chen, J. Zhou, S.-T. Zhang, M.-H. Lu, and Y.-F. Chen, Extremely large and significantly anisotropic magnetoresistance in ZrSiS single crystals. Appl. Phys. Lett. **108**, 244101 (2016).

[7] X. Luo, R. C. Xiao, F. C. Chen, J. Yan, Q. L. Pei, Y. Sun, W. J. Lu, P. Tong, Z. G. Sheng, X. B. Zhu, W. H. Song, and Y. P. Sun, Origin of the extremely large magnetoresistance in topological semimetal $PtSn_4$. Phys. Rev. B **97**, 205132 (2018).

[8] K. Okawa, M. Kanou, H. Namiki, and T. Sasagawa, Extremely large magnetoresistance induced by hidden three-dimensional Dirac bands in nonmagnetic semimetal InBi. Phys. Rev. Mater. **2**, 124201 (2018).

[9] M. Novak, S. N. Zhang, F. Orbanić, N. Biliškov, G. Eguchi, S. Paschen, A. Kimura, X. X. Wang,

T. Osada, K. Uchida, M. Sato, Q. S. Wu, O. V. Yazyev, and I. Kokanović, Highly anisotropic interlayer magnetoresitance in ZrSiS nodal-line Dirac semimetal. Phys. Rev. B **100**, 085137 (2019).

[10] Y. Wu, N. H. Jo, M. Ochi, L. Huang, D. Mou, S. L. Bud'ko, P. C. Canfield, N. Trivedi, R. Arita, and A. Kaminski, Temperature-induced Lifshitz transition in WTe_2. Phys. Rev. Lett. **115**, 166602 (2015).

[11] Y. Luo, H. Li, Y. M. Dai1, H. Miao, Y. G. Shi, H. Ding, A. J. Taylor, D. A. Yarotski, R. P. Prasankumar, and J. D. Thompson, Hall effect in the extremely large magnetoresistance semimetal WTe_2. Appl. Phys. Lett. **107**, 182411 (2015).

[12] J. Wang, H. Yang, L. Ding, W. You, C. Xi, J. Cheng, Z. Shi, C. Cao, Y. Luo, Z. Zhu, J. Dai, M. Tian and Y. Li, Angle-dependent magnetoresistance and its implications for Lifshitz transition in W_2As_3. npj Quant. Mater. **4**, 58 (2019).

[13] F. C. Chen, Y. Fei, S. J. Li, Q. Wang, X. Luo, J. Yan, W. J. Lu, P. Tong, W. H. Song, X. B. Zhu, L. Zhang, H. B. Zhou, F. W. Zheng, P. Zhang, A. L. Lichtenstein, M. I. Katsnelson, Y. Yin, Ning Hao, and Y. P. Sun, Temperature-induced Lifshitz transition and possible excitonic instability in ZrSiSe. Phys. Rev. Lett. **124**, 236601 (2020).

[14] P. B. Person, Electrical resistivity, Hall coefficient, and thermoelectric power of $AuSb_2$ and Cu_2Sb. Can. J. Phys. **42**, 519 (1964).

[15] K. Andres, E. Bucher, J.P. Maita, and A. S. Cooper, Superconductivity of CuSb phases and absence of antiferromagnetism in Cu_2Sb. Phys. Lett. A **28**, 67 (1968).

[16] L. C. Gupta, S. K. Malik, and R.Vijayaraghavan, NMR evidence to the absence of antiferromagnetism in Cu_2Sb. Phys. Lett. A **28**, 255 (1968).

[17] J.-P. Jan and R. M. Boulet, The de Haas-van Alphen effect in the intermetallic compound Cu_2Sb. J. Low Temp. Phys. **8**, 305 (1972).

[18] D. J. Sellmyer, F. R. Szofran and J. W. Weymouth, Magnetoresistance of the metallic compounds Cu_2Sb and YZn to 220 kG. J. Low Temp. Phys. **18**, 85 (1975).

[19] J.-P. Jan, H. L. Skriver, Band structure and Fermi surface of Cu_2Sb by the LMTO method. J. Phys. F: Metal Phys. **7**, 957 (1977).

[20] T. Ito, M. Shirai, and K. Motizuki, Electronic band structures of intermetallic compound Cu_2Sb. J. Phys. Soc. Jpn. **61**, 2202 (1992).

[21] F. Izumi and K. Momma, Three-dimensional visualization in powder diffraction. Solid State Phenom. **130**, 15 (2007).

[22] K. Momma and F. Izumi, VESTA 3 for three-dimensional visualization of crystal, volumetric and morphology data. J. Appl. Crystallogr. **44**, 1272 (2011).

[23] T. Oguchi, Augmented-plane-wave force calculations for transition-metal systems, "Inter-atomic Potentials and Structural Stability", ed. K. Terakura and H. Akai, (Springer-Verlag, 1993) p. 33.

[24] J. P. Perdew, J. A. Chevary, S. H. Vosko, Koblar A. Jackson, Mark R. Pederson, D. J. Singh, and Carlos Fiolhais, Atoms, molecules, solids, and surfaces: Applications of the generalized gradient approximation for exchange and correlation. Phys. Rev. B **46**, 6671 (1992).

[25] P. E. Blöchl, O. Jepsen, and O. K. Andersen, Improved tetrahedron method for Brillouin-zone integrations. Phys. Rev. B **49**, 16223 (1994).

[26] M. Kawamura, FermiSurfer: Fermi-surface viewer providing multiple representation schemes. Comp. Phys. Commun. **239**, 197 (2019).

[27] See Supplemental Material for crystal structural parameters, powder XRD pattern, magnetic susceptibility, raw data of Hall resistance, fitting results of two carrier model, angular dependence of magnetoresistance for ρ_{xx}, comparison of the ARPES intensity at T = 13 and 40 K, and k_z broadening effect in the ARPES data.

[28] M. Yuzuri, On the magnetic properties of Cr_2As and Cu_2Sb. J. Phys. Soc. Jpn. **15**, 2007 (1960).

[29] A. B. Pippard, Magnetoresistance in metals (Cambridge University Press, New York, 1989).

[30] M. P. Seah and W. A. Dench, Quantitative electron spectroscopy of surfaces: A standard data base for electron inelastic mean free paths in solids. Surf. Interface Anal. **1**, 2 (1979).

[31] H. Kumigashira, Hyeong-Do Kim, T. Ito, A. Ashihara, T. Takahashi, T. Suzuki, M. Nishimura, O. Sakai, Y. Kaneta, and H. Harima, High-resolution angle-resolved photoemission study of LaSb, Phys. Rev. B **58**, 7675 (1998).

[32] W. Setyawan and Stefano Curtarolo, Comp. Meter. Sci. **49**, 299 (2010).

Figures

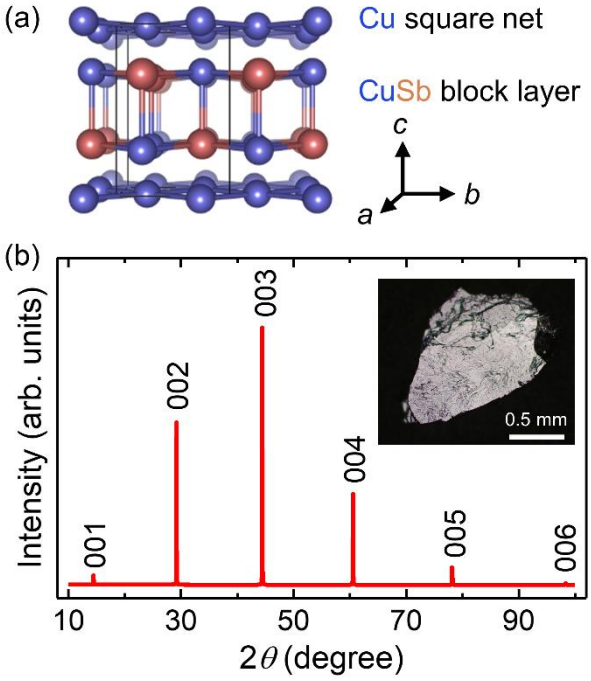

FIG. 1. (a) Crystal structure of Cu_2Sb. (b) XRD pattern of Cu_2Sb single crystal. Inset shows the photograph of Cu_2Sb single crystal cleaved along *ab*-plane.

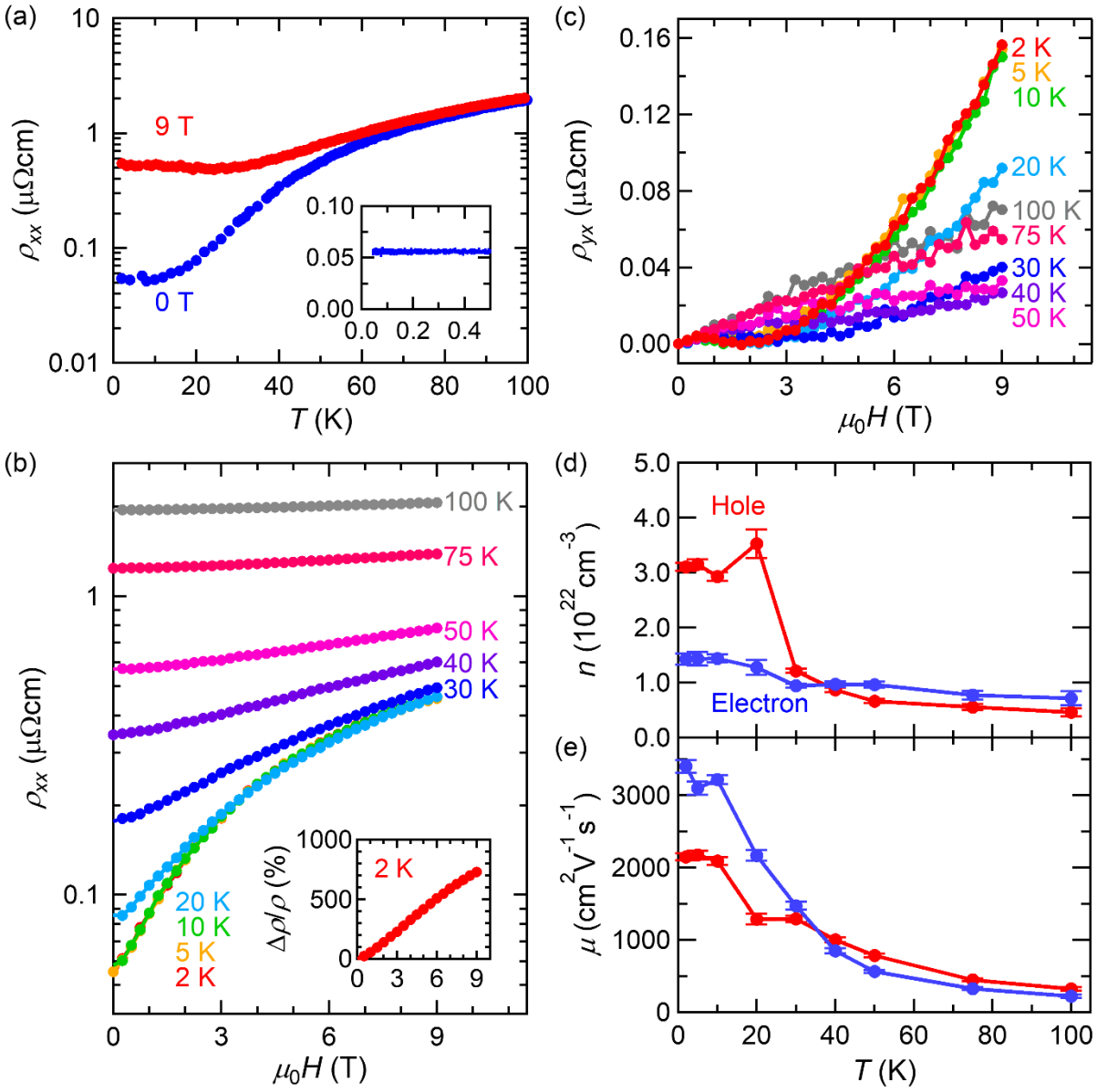

FIG. 2. (a) Temperature dependence of resistivity along *a*-axis (ρ_{xx}) at 0 T (blue) and 9 T (red) for Cu_2Sb. The magnetic field was applied along *c*-axis. Inset shows a magnified view below 0.4 K. Magnetic field dependence of (b) ρ_{xx} and (c) ρ_{yx} at various temperatures. Inset in (b) shows magnetic field dependence of magnetoresistance for ρ_{xx} at 2 K. Temperature dependence of (d) carrier density and (e) mobility of electron (blue) and hole (red) carriers for Cu_2Sb. The fitting results were shown in Table S2, Figs. S4 and S5 in the Supplemental Material [27].

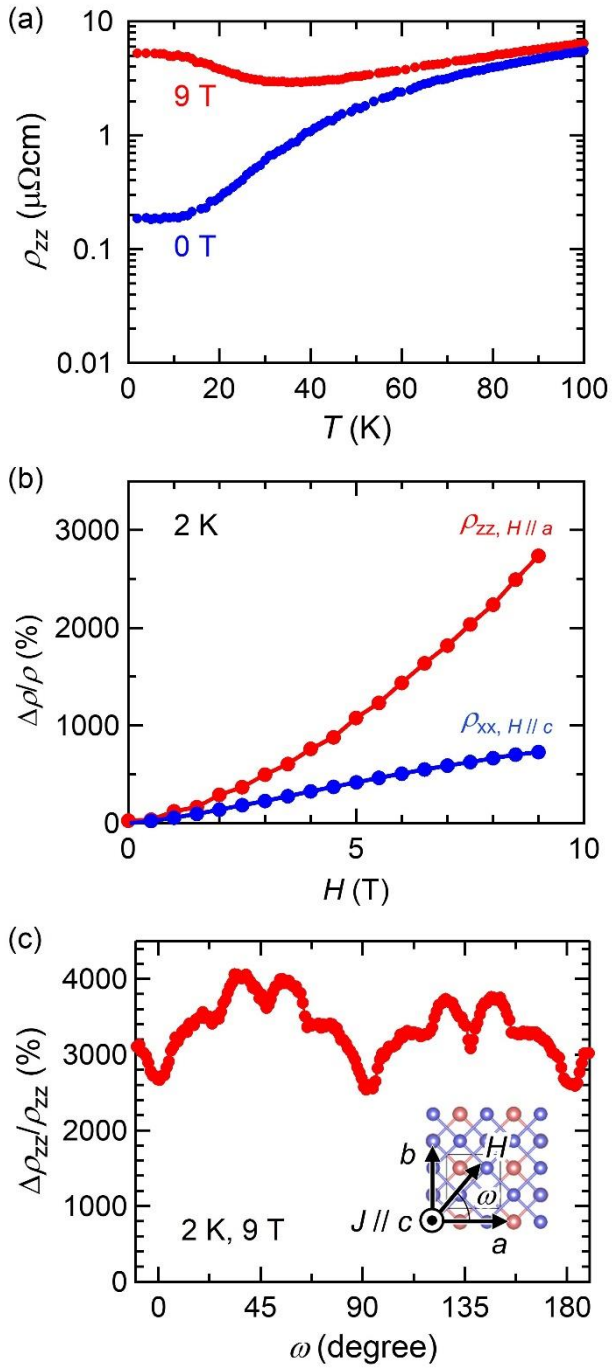

FIG. 3. (a) Temperature dependence of resistivity along *c*-axis (ρ_{zz}) at 0 T (blue) and 9 T (red) for Cu_2Sb. The magnetic field was applied along *a*-axis. (b) Magnetic field dependence of magnetoresistance for ρ_{xx} (blue) and ρ_{zz} (red) at 2 K. The magnetic field applied along *c*- and *a*- axis for ρ_{xx} and ρ_{zz}, respectively. (c) Angular dependence of magnetoresistance at 2 K and 9 T for ρ_{zz}. Magnetic field was rotated in the *ab*- plane. The inset denotes the measurement geometry.

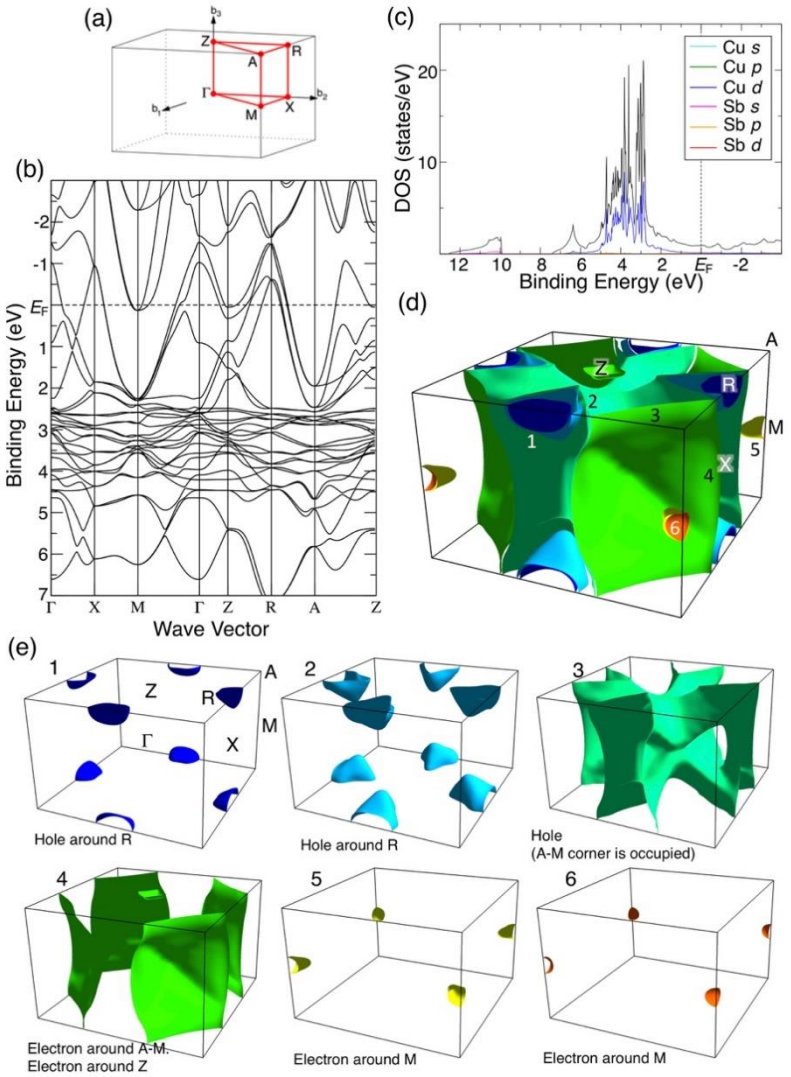

FIG. 4. (a) Bulk Brillouin zone of Cu_2Sb. The *k*-point path (red lines) is taken from AFLOW program [32]. (b) Calculated band structure along high symmetry lines in the bulk Brillouin zone. All the bands are doubly degenerate due to the space-inversion symmetry and the time-reversal symmetry. (c) Plot of calculated partial and total density of states (DOS) as a function of E_B. (d) 3D plot of calculated Fermi surfaces in the bulk Brillouin zone. (e) Fermi-surface plots for each band in separate panels where the occupied side of the surfaces is illuminated. The Fermi surfaces were drawn by using FermiSurfer program [26].

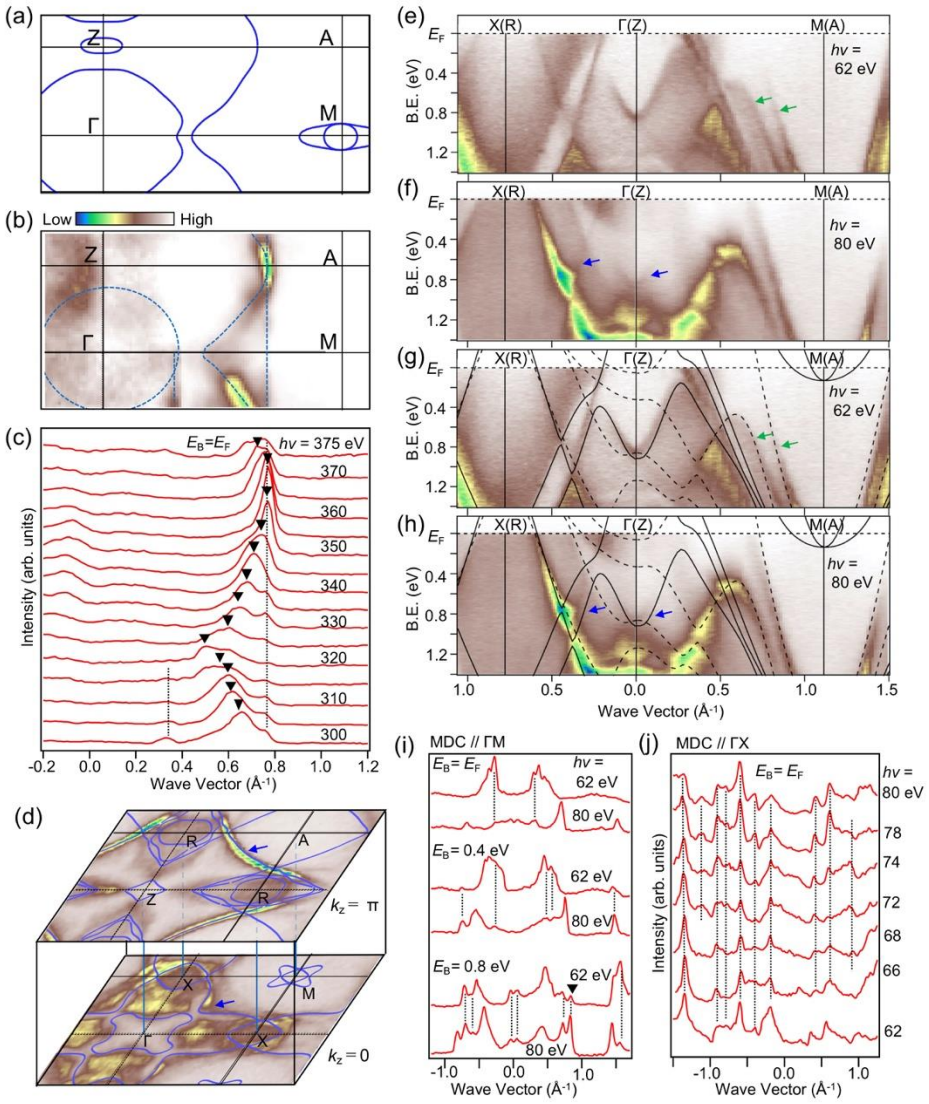

FIG. 5. (a) Calculated Fermi surface in the ΓMAZ plane. (b) ARPES intensity at E_F plotted as a function of $k_{//}$ (parallel to the ΓM cut) and k_z measured by varying $h\nu$ with SX photons ($h\nu$ = 300–375 eV). ARPES intensity at E_F is obtained by integrating the intensity within ± 30 meV of E_F. Dashed curves are guides to the eyes to trace the experimental Fermi surface. (c) Corresponding MDC at E_F. Triangles indicate the quasi-2D band originating from band 4, whereas dashed vertical lines show 2D-like bands. (d) ARPES-intensity mapping at E_F at $k_z \sim 0$ (bottom) and $k_z \sim \pi$ (top). Calculated Fermi surfaces are also overlaid. Blue arrows indicate the quasi-2D pocket from band 4. (e), (f) ARPES intensity plotted as a function of wave vector and binding energy measured along the XΓM cut (k_z = 0 plane) at $h\nu$ = 62 eV and the RZA cut (k_z = π plane) at $h\nu$ = 80 eV, respectively. (g), (h) Same as (e) and (f) but calculated band structures along k_z = 0 and π is also overlaid. (i) MDCs along the ΓM cut at E_B = E_F, 0.4, and 0.8 eV measured with VUV photons of $h\nu$ = 62 and 80 eV. (j) MDCs at E_F along the ΓX cut at different $h\nu$'s in a VUV region (62–80 eV).